

A highly active repeating fast radio burst in a complex local environment

Di Li (✉ dili@nao.cas.cn)

National Astronomical Observatories, Chinese Academy of Sciences <https://orcid.org/0000-0003-3010-7661>

C.H. Niu

National Astronomical Observatories, Chinese Academy of Sciences

Kshitij Aggarwal

West Virginia University <https://orcid.org/0000-0002-2059-0525>

Xian Zhang

Shang Hai AO

Shami Chatterjee

Cornell University <https://orcid.org/0000-0002-2878-1502>

Chao-Wei Tsai

National Astronomical Observatories, Chinese Academy of Sciences, Beijing 100101, China

Wenfei Yu

Shanghai Astronomical Observatory

Casey Law

Cahill Center for Astronomy and Astrophysics, MC 249-17 California Institute of Technology, Pasadena, CA 91125, USA

Sarah Burke-Spolaor

Department of Physics and Astronomy, West Virginia University; Center for Gravitational Waves and Cosmology, West Virginia University; Canadian Institute for Advanced Research, CIFAR Azrieli Global

James Cordes

Cornell

Yongkun Zhang

National Astronomical Observatories, Chinese Academy of Sciences, Beijing 100101, China

Stella Ocker

Cornell Center for Astrophysics and Planetary Science <https://orcid.org/0000-0002-4941-5333>

Jumei Yao

National Astronomical Observatories, Chinese Academy of Sciences, Beijing 100101, China

P. Wang

National Astronomical Observatories, Chinese Academy of Sciences

Yi Feng

National Astronomical Observatories, Chinese Academy of Sciences, Beijing 100101, China

Yuu Niino

Institute of Astronomy, Graduate School of Science, The University of Tokyo, 2-21-1 Osawa, Mitaka, Tokyo 181-0015, Japan

Christopher Bochenek

Caltech <https://orcid.org/0000-0003-3875-9568>

Marilyn Cruces

Max-Planck-Institut für Radioastronomie, Auf dem Hügel 69, D-53121 Bonn, Germany

Liam Connor

Cahill Center for Astronomy and Astrophysics

Ji-an Jiang

Kavli Institute for the Physics and Mathematics of the Universe, The University of Tokyo, 5-1-5 Kashiwanoha, Kashiwa, Chiba, 277-8583, Japan

Shi Dai

CSIRO Space and Astronomy, PO Box 76, Epping, NSW 1710, Australia

Rui Luo

CSIRO <https://orcid.org/0000-0002-4300-121X>

Guodong Li

National Astronomical Observatories, Chinese Academy of Sciences, Beijing 100101, China

C.C. Miao

National Astronomical Observatories, Chinese Academy of Sciences

J.R. Niu

National Astronomical Observatories, Chinese Academy of Sciences

Reshma Anna-Thomas

Department of Physics and Astronomy, West Virginia University; Center for Gravitational Waves and Cosmology, West Virginia University

Daniel Stern

Jet Propulsion Laboratory, California Institute of Technology

Weiyang Wang

National Astronomical Observatories, Chinese Academy of Sciences, Beijing 100101, China; Department of Astronomy, School of Physics, Peking University, Beijing 100871, China

Mao Yuan

National Astronomical Observatories, Chinese Academy of Sciences, Beijing 100101, China

Youling Yue

National Astronomical Observatories, Chinese Academy of Sciences <https://orcid.org/0000-0003-4415-2148>

D.J. Zhou

National Astronomical Observatories, Chinese Academy of Sciences

Zhen Yan

Shang Hai AO

Weiwei Zhu

Chinese Academy of Sciences <https://orcid.org/0000-0001-5105-4058>

Bing Zhang

Department of Physics and Astronomy, University of Nevada, Las Vegas, Las Vegas, NV 89154,USA

Physical Sciences - Article

Keywords: fast radio bursts (FRB), planetary science, plasma

Posted Date: July 28th, 2021

DOI: <https://doi.org/10.21203/rs.3.rs-745622/v1>

License:  This work is licensed under a Creative Commons Attribution 4.0 International License.

[Read Full License](#)

A highly active repeating fast radio burst in a complex local environment

C.-H. Niu¹*, K. Aggarwal^{2,6}*, ✉D. Li^{1,11}*, X. Zhang^{3,11}, S. Chatterjee⁴, C.-W. Tsai¹, ✉W. Yu³, ✉C. J. Law^{5,8}, S. Burke-Spolaor^{2,6,7}, J. M. Cordes⁴, Y.-K. Zhang^{1,11}, S. Ocker⁴, J.-M. Yao^{1,12}, P. Wang¹, Y. Feng^{1,11}, Y. Niino^{9,19}, C. Bochenek⁵, M. Cruces¹⁶, L. Connor⁵, J.-A. Jiang¹⁷, S. Dai^{13,18}, R. Luo¹³, G.-D. Li^{1,11}, C.-C. Miao^{1,11}, J.-R. Niu^{1,11}, R. Anna-Thomas^{2,6}, D. Stern¹⁰, W.-Y. Wang^{1,14}, M. Yuan^{1,11}, Y.-L. Yue¹, D.-J. Zhou^{1,11}, Z. Yan³, W.-W. Zhu¹, B. Zhang¹⁵

¹*National Astronomical Observatories, Chinese Academy of Sciences, Beijing 100101, China*

²*Department of Physics and Astronomy, West Virginia University, P.O. Box 6315, Morgantown, WV 26506, USA*

³*Shanghai Astronomical Observatory, Chinese Academy of Sciences, 80 Nandan Road, Shanghai 200030, China*

⁴*Cornell Center for Astrophysics and Planetary Science, and Department of Astronomy, Cornell University, Ithaca, NY 14853, USA*

⁵*Cahill Center for Astronomy and Astrophysics, MC 249-17 California Institute of Technology, Pasadena, CA 91125, USA*

⁶*Center for Gravitational Waves and Cosmology, West Virginia University, Chestnut Ridge Research Building, Morgantown, WV 26505, USA*

✉Email:dili@nao.cas.cn

✉Email:wenfei@shao.ac.cn

✉Email:claw@astro.caltech.edu

*These authors contributed equally to this work.

20 ⁷*Canadian Institute for Advanced Research, CIFAR Azrieli Global Scholar, MaRS Centre West*
21 *Tower, 661 University Ave. Suite 505, Toronto ON M5G 1M1, Canada*

22 ⁸*Owens Valley Radio Observatory, California Institute of Technology, Pasadena, CA 91125, USA*

23 ⁹*Institute of Astronomy, Graduate School of Science, The University of Tokyo, 2-21-1 Osawa,*
24 *Mitaka, Tokyo 181-0015, Japan*

25 ¹⁰*Jet Propulsion Laboratory, California Institute of Technology, 4800 Oak Grove Drive, M/S 264-*
26 *723, Pasadena, CA 91109, USA*

27 ¹¹*University of Chinese Academy of Sciences, Beijing 100049, China*

28 ¹²*Xinjiang Astronomical Observatory, Chinese Academy of Sciences, 150, Science 1-Street,*
29 *Urumqi, Xinjiang 830011, China*

30 ¹³*CSIRO Space and Astronomy, PO Box 76, Epping, NSW 1710, Australia*

31 ¹⁴*Department of Astronomy, School of Physics, Peking University, Beijing 100871, China*

32 ¹⁵*Department of Physics and Astronomy, University of Nevada, Las Vegas, Las Vegas, NV 89154,*
33 *USA*

34 ¹⁶*Max-Planck-Institut für Radioastronomie, Auf dem Hügel 69, D-53121 Bonn, Germany*

35 ¹⁷*Kavli Institute for the Physics and Mathematics of the Universe (WPI), The University of Tokyo,*
36 *5-1-5 Kashiwanoha, Kashiwa, Chiba 277-8583, Japan*

37 ¹⁸*School of Science, Western Sydney University, Locked Bag 1797, Penrith South DC, NSW 2751,*
38 *Australia*

39 ¹⁹*Research center for the early universe, The University of Tokyo, Hongo, 7-3-1, Bunkyo-ku,*
40 *Tokyo, 113-0033, Japan*

41 **The central engine of fast radio bursts (FRB) is not yet understood. Due to the interaction be-**
42 **tween the pulse and the intervening plasma, the dispersion sweep of FRBs provides a unique**
43 **probe of its environment and the ionized baryon content of the intergalactic medium¹. Ac-**
44 **tive repeaters has been shown to be associated with persistent radio source² (PRS), and dense,**
45 **energetic, magnetized plasmas^{3,4}. Here we report the discovery and localization of a new, ex-**
46 **tremely active repeater, FRB 190520, which is co-located with a compact PRS and identified**
47 **with a dwarf host galaxy of high star formation at a redshift $z = 0.241$. The estimated host**
48 **galaxy contribution $DM_{\text{host}} \approx 912_{-108}^{+69} \text{ pc cm}^{-3}$ is nearly an order of magnitude higher than the**
49 **average of FRB host galaxies^{5,6} and much larger than the contribution from the intergalac-**
50 **tic medium, suggesting caution in inferring redshifts for FRBs without accurate host galaxy**
51 **identifications. This represents the second source after FRB 121102 with confirmed associa-**
52 **tion between FRB and compact PRS. The dense, complex host galaxy environment and the**
53 **associated persistent radio source may point to a distinctive origin or an earlier evolutionary**
54 **stage for highly active repeating FRBs.**

55 FRB 190520 was discovered with the Five-hundred-meter Aperture Spherical radio Tele-
56 scope (FAST)⁷ in drift-scan mode as part of the Commensal Radio Astronomy FAST Survey
57 (CRAFTS⁸) at 1.05–1.45 GHz in 2019. Four bursts were detected during the initial scan, iden-
58 tifying it as a repeater. Monthly follow-up tracking observations between 2020 April and 2020
59 September detected 75 bursts in 18.5 hrs at a mean pulse dispersion measure (DM) of $1202 \pm$
60 10 pc cm^{-3} . Assuming a Weibull distribution of the burst waiting time, we model the FRB burst
61 rate to be $R(7\sigma > 9.3 \text{ mJy ms}) = 4.5_{-1.5}^{+1.9} \text{ hr}^{-1}$, making it one of the most active repeating FRBs

62 detected to date^{9,10}. Similar to other repeaters, this FRB shows complex frequency-time structure,
63 with frequency modulation, multi-component-profiles, sub-burst drifting, and scattering (Figure 1
64 and Methods).

65 We observed FRB 190520 with the Karl G. Jansky Very Large Array (VLA) using the *real-*
66 *fast* fast transient detection system¹¹. Throughout the second half of 2020, we observed the source
67 for 16 hours and detected 3, 5, and 1 bursts in bands centered at 1.5 GHz, 3 GHz, and 5.5 GHz,
68 respectively. We measured a burst source position of (RA, Dec)[J2000] = (16h02m04.268s±0.12",
69 -11°17'17.32"±0.12") with position uncertainty (1σ) dominated by systematic effects. Deep im-
70 ages using data from the same observing campaign reveal a compact persistent radio source (PRS)
71 at (RA,Dec)[J2000] = (16h02m04.2611s±0.124", -11°17'17.3869"±0.126") (statistical plus sys-
72 tematic errors) and flux density of $202 \pm 8 \mu\text{Jy}$ at 3.0 GHz. Using averaged flux density at each
73 sub-band over the VLA campaign, we find a PRS flux density spectrum can be fit with a powerlaw
74 with index -0.41 ± 0.04 .

75 Figure 2 shows the FRB location compared to deep optical, near-infrared (NIR) and radio
76 images of the field. The optical image (*R'*-band) obtained by CFHT/MegaCam reveals a galaxy
77 (J160204.31–111718.5) at the location of the FRB, the light profile of which peaks at $\sim 1''$ south
78 east. Given the measured offset of the FRB from the galaxy and the density of galaxies with
79 this magnitude, we estimate a chance coincidence probability of less than 1%^{12,13}, supporting
80 J160204.31–111718.5's being the host galaxy of FRB 190520. The NIR image (*J*-band) obtained
81 by Subaru/MOIRCS¹⁴ shows the most likely stellar component of J160204.31–111718.5 with an

82 AB magnitude of 22.1 ± 0.1 in J -band, with FRB 190520 and the PRS on the galaxy periphery.

83 We obtained an optical spectrum at the location of the FRB with the Double Spectrograph on
84 the Palomar 200-inch Hale Telescope that revealed the redshift of the putative host to be $z = 0.241$
85 based on a detection of strong $H\alpha$, [O III] 4859Å, and [O III] 5007Å lines (see Methods). A follow-
86 up observation with the Low Resolution Imaging Spectrometer (LRIS) at the Keck I Telescope
87 covering both the FRB location and the nearby Subaru J -band source along the extended R -band
88 structure indicates the R' -band structure is dominated by the [O III] emission at the same redshift
89 of $z = 0.241$. The $H\alpha$ luminosity $L_{H\alpha} = 7.4 \pm 0.2 \times 10^{40}$ erg sec $^{-1}$ after extinction correction
90 suggests a star formation rate of $\sim 0.41 M_{\odot}$ yr $^{-1}$. Based on the J -band magnitude, we estimate the
91 stellar mass of the host galaxy to be $\sim 6 \times 10^8 M_{\odot}$. Thus, we characterize J160204.31–111718.5
92 as a dwarf galaxy with a relatively high star-formation rate for its stellar mass¹⁵. At the luminosity
93 distance implied by the redshift, the PRS has a radio luminosity of $L_{3 \text{ GHz}} = 4 \times 10^{29}$ erg cm $^{-1}$
94 Hz $^{-1}$.

95 It is usually assumed that the redshift of a FRB source can be estimated from the DM at-
96 tributed to the intergalactic medium (IGM), $DM_{\text{IGM}} = DM_{\text{FRB}} - DM_{\text{host}} - DM_{\text{MW}}$. Theoretical
97 calculations¹⁶ and observations¹ have independently estimated the IGM contribution to FRB DM
98 as a function of redshift (Figure 3). For nominal DM contributions from the Milky Way (100
99 pc cm $^{-3}$ for MW disk and MW halo) and host galaxy (50 pc cm $^{-3}$) and also assuming baryon frac-
100 tions of 0.6 to 1 for the ionized IGM, the implied redshift range for FRB 190520 is $z \sim 1$ to 1.6,
101 which is much larger than the measured value. Instead, using $DM_{\text{IGM}}(z = 0.241)$ with 50% scatter

102 about a mean of 200 pc cm^{-3} (to account for cosmic variance of DM_{IGM} for a baryon fraction of
 103 0.8) combined with a Milky Way contribution $\text{DM}_{\text{MW}} = 60 \text{ pc cm}^{-3}$ with a 20% error based on
 104 the NE2001¹⁷ electron density model for the disk and marginalized over a Milky-Way-halo con-
 105 tribution of 25 to 80 pc cm^{-3} , a very high host DM (disk + circumgalaxy contribution) of 912_{-108}^{+69}
 106 pc cm^{-3} is implied.

107 The measured DM and scattering properties exclude the possibility that J160204.31–111718.5
 108 is a foreground galaxy with the true FRB host much further in the background. If this were the case,
 109 the observed $\text{H}\alpha$ emission would imply an estimated mean DM contribution of about 474 pc cm^{-3}
 110 from the foreground galaxy in the observer frame (for a nominal temperature $T \sim 10^4 \text{ K}$; see Meth-
 111 ods), and the corresponding DM budget would imply a host galaxy at a redshift $z \sim 0.5$. The scat-
 112 tering contribution of the foreground galaxy is related to its DM contribution by $\tau \propto \tilde{F} \times G \times \text{DM}^2$,
 113 where \tilde{F} describes the density fluctuation statistics in the ionized medium and G is a geometric
 114 factor relating the relative distances between the source, lens, and observer (see Methods). For a
 115 DM contribution of 474 pc cm^{-3} , a host galaxy at redshift $z \sim 0.5$, and a lens galaxy at a redshift
 116 $z_\ell = 0.241$, the predicted scattering time is $\tau \approx 3 \text{ s}$ at 1375 MHz, orders of magnitude larger than
 117 the observed scattering time of 10.8 ms. The observed scattering time is thus far too small for the
 118 proposed host galaxy to lie in the foreground.

119 The use of FRBs as probes of baryons in the IGM requires estimating the contributions to
 120 the pulse DM from the Milky Way and the host galaxy. So far, it has been assumed that the host
 121 DM is dominated by the interstellar medium of the galaxy, which could be modeled, estimated

122 from observations, or simply averaged in a statistical sense for an ensemble of observations. FRB
123 190520 shows that the distribution of DM_{host} values can have a long tail, which adds considerable
124 variance to estimates for the IGM.

125 The co-located compact PRS, the star-forming dwarf host galaxy, and the high repetition
126 rate, make FRB 190520 a clear analog to FRB 121102, the first repeating FRB¹⁸ and the first
127 to be identified with a luminous PRS² ($L_{\nu} = 2 \times 10^{29} \text{ erg s}^{-1} \text{ Hz}^{-1}$). Another repeating source,
128 FRB 201124A, was also associated with persistent radio emission^{19–21}. However, through optical
129 spectroscopy and radio interferometric measurements, it was demonstrated that the persistent radio
130 emission was spatially extended and consistent with radio emission from star formation in the host
131 galaxy²². If the persistent radio emission associated with FRB 190520 is from star formation,
132 however, the PRS luminosity would imply a star-formation rate of $\sim 10 M_{\odot} \text{ yr}^{-1}$, a factor of 25
133 larger than that measured for the host galaxy. Given the extreme PRS luminosity, its unresolved
134 structure in VLA observations, and its offset from the center of the optical emission of the host
135 galaxy, we conclude that the PRS is a compact source that is physically connected to the FRB
136 190520, as found for FRB 121102².

137 Burst repetition and spectral structure have been used to argue that repeating and non-
138 repeating FRBs comprise subclasses²³, either at different evolutionary phases or entirely different
139 physical scenarios. The observed burst properties are subject to observational biases²⁴, but PRS
140 emission and DM_{host} reflect different aspects of the FRB environment.

141 Prior to FRB 190520, more than a dozen FRBs had been localized, including five repeat-

142 ing sources^{25,26}, but only FRB 121102 had been found to be associated with a compact PRS. The
143 two FRBs associated with PRSs are among the most active (e.g. a peak burst rate of 117 hr^{-1}
144 has been found for FRB 121102²⁷) and have large DM_{host} values, implying that they may be fea-
145 tures of active FRBs that requires dense, magnetized plasma within parsecs of the source of the
146 bursts^{10,28}. Burst activity may then be correlated with the relativistic plasma emitting synchrotron
147 radiation and the presence of thermal plasma in the local FRB environment. The nature of that
148 correlation is plausibly related to FRB formation (e.g., a newborn source in a young supernova
149 remnant or relativistic wind nebula), suggesting that highly active repeaters, such as FRB 121102
150 and FRB 190520, are “newborns”, which still reside in their complex, natal environments^{28,29}. In
151 this scenario, as the source ages, the PRS fades, the event rate drops, and the surrounding plasma
152 dissipates³⁰.

153 The discovery of FRB 190520 and its high similarity to FRB 121102 demonstrate that some
154 FRBs have very large local DM and PRS counterparts. We expect more such detections in the
155 near future to distinguish between two scenarios: that active repeaters and non-repeaters are dis-
156 tinctive populations, or that both repeating and apparently non-repeating FRBs are produced by a
157 single source population at different evolutionary stages. Either possibility has direct impact on
158 calibrating the FRB DM as a probe of cosmic baryons and on understanding FRB origin(s).

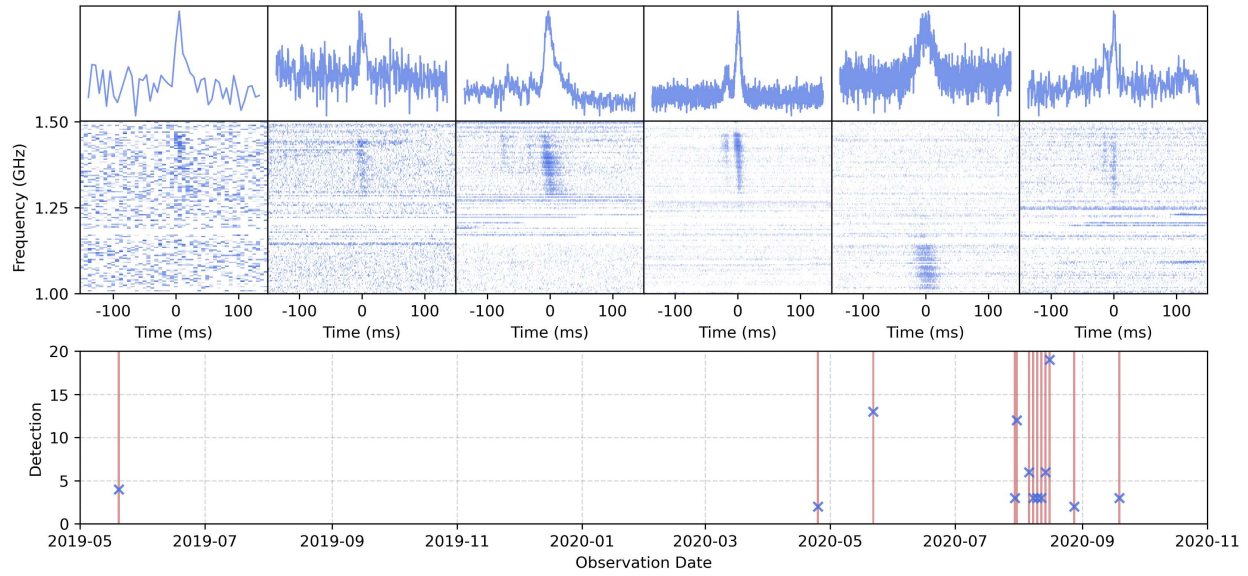


Figure 1: Top row: Frequency integrated burst intensities of six bursts detected during FAST observations. Middle: De-dispersed dynamic spectra of the bursts clearly showing the band-limited nature of these bursts. Darker patches represent higher intensities. Bottom: The number of bursts detected at each epoch. The red lines span the observation windows of that day and the blue crosses represent the number of bursts detected in that observation.

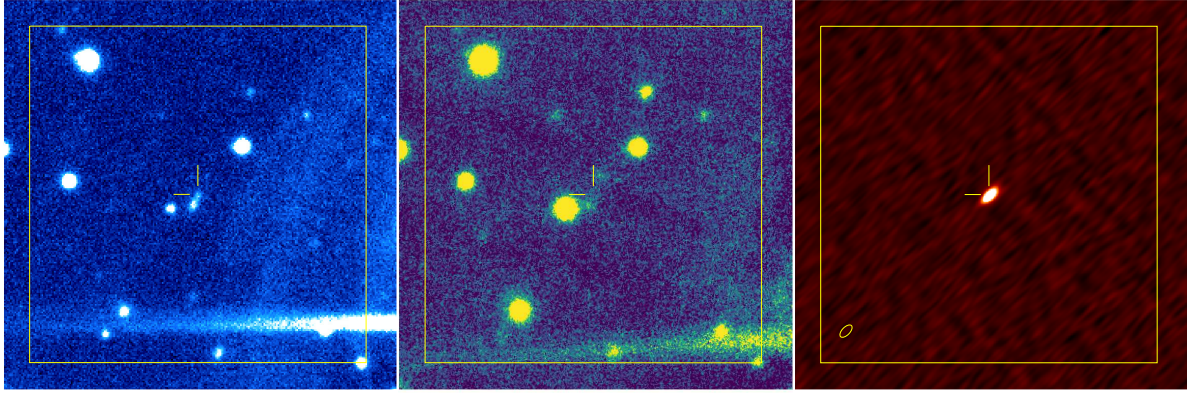


Figure 2: Optical, infrared, and radio images of the field of FRB 190520. In each case, the box is $40''$ in size and the $2''$ crosshairs indicate the best FRB position at $16^{\text{h}} 02^{\text{m}} 04.2683\text{s} - 11^{\circ} 17' 17''.3203$. (Left) An optical R' -band image obtained by CFHT MegaCam covers $5427\text{\AA} - 7041\text{\AA}$, including redshifted $\text{H}\beta$ 4861\AA , $[\text{OIII}]4959\text{\AA}$, and $[\text{OIII}]5007\text{\AA}$ emission lines from the host galaxy. (Middle) The infrared J -band image by Subaru/MOIRCS shows emission only at the location of the peak of the optical light profile of the host galaxy. (Right) The radio VLA image ($2-4$ GHz) shows a compact persistent source at the FRB location. The synthesized beam is shown as an ellipse of size $(0'.92 \times 0'.47)$ in the left corner.

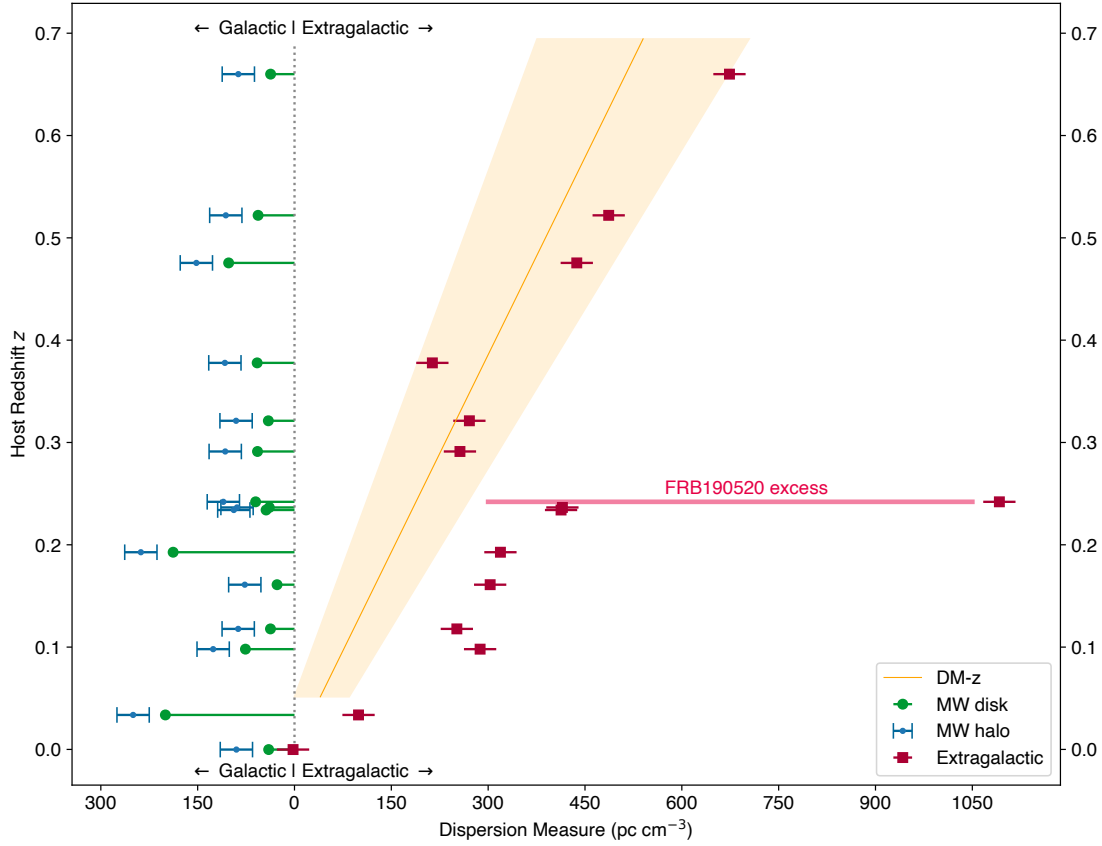


Figure 3: Galactic and extragalactic contributions to the DM observed for FRBs with firm host galaxy associations and redshifts, adapted from ref. ³¹. Galactic disk contributions are estimated from NE2001¹⁷ with an additional halo contribution of $50 \pm 25 \text{ pc cm}^{-3}$ (full range; this range is also reflected in the error bars plotted for the extragalactic DM). The expected DM contribution of the intergalactic medium (orange line) is $972 \text{ pc cm}^{-3} f_{\text{IGM}} f(z)$, where $f(z) \approx 1.06z$ at $z \sim 0.24$ and the baryonic fraction in the ionized IGM is $f_{\text{IGM}} \sim 0.8$, with a 1σ band $\sim \sqrt{50 \times \text{DM}_{\text{IGM}}} \text{ pc cm}^{-3}$ due to cosmic variance. The host galaxy contributions DM_{host} shift observed values to the right of the band of extragalactic DM predicted for the intergalactic medium alone. FRB 190520 is a clear outlier from the general trend, with an unprecedented DM contribution from its host galaxy.

- 189 1. Macquart, J.-P. et al. A census of baryons in the universe from localized fast radio bursts.
161 Nature **581**, 391–395 (2020).
- 162 2. Chatterjee, S. et al. A direct localization of a fast radio burst and its host. Nature **541**, 58–61
163 (2017). 1701.01098.
- 164 3. Masui, K. et al. Dense magnetized plasma associated with a fast radio burst. Nature **528**,
165 523–525 (2015). 1512.00529.
- 166 4. Michilli, D. et al. An extreme magneto-ionic environment associated with the fast radio burst
167 source FRB 121102. Nature **553**, 182–185 (2018). 1801.03965.
- 168 5. Luo, R., Lee, K., Lorimer, D. R. & Zhang, B. On the normalized FRB luminosity function.
169 Mon. Not. R. Astron. Soc. **481**, 2320–2337 (2018). 1808.09929.
- 170 6. Niino, Y. Dispersion measure components within host galaxies of Fast Radio Bursts: observa-
171 tional constraints from statistical properties of FRBs. arXiv e-prints arXiv:2005.12891 (2020).
172 2005.12891.
- 173 7. NAN, R. et al. The five-hundred-meter aperture spherical radio telescope (fast) project.
174 International Journal of Modern Physics D **20**, 989–1024 (2011).
- 175 8. Li, D., Dickey, J. M. & Liu, S. Preface: Planning the scientific applications of the five-
176 hundred-meter aperture spherical radio telescope. Research in Astronomy and Astrophysics
177 **19**, 016 (2019). URL <http://dx.doi.org/10.1088/1674-4527/19/2/16>.

- 178 9. Chime/Frb Collaboration et al. Periodic activity from a fast radio burst source. *Nature* **582**,
179 351–355 (2020). 2001.10275.
- 180 10. Cruces, M. et al. Repeating behaviour of FRB 121102: periodicity, waiting times, and energy
181 distribution. *Mon. Not. R. Astron. Soc.* **500**, 448–463 (2021). 2008.03461.
- 182 11. Law, C. J. et al. realfast: Real-time, Commensal Fast Transient Surveys with the Very Large
183 Array. *Astrophys. J. Suppl.* **236**, 8 (2018). 1802.03084.
- 184 12. Bloom, J. S., Kulkarni, S. R. & Djorgovski, S. G. The Observed Offset Distribution of
185 Gamma-Ray Bursts from Their Host Galaxies: A Robust Clue to the Nature of the Progenitors.
186 *Astron. J.* **123**, 1111–1148 (2002). astro-ph/0010176.
- 187 13. Eftekhari, T. & Berger, E. Associating Fast Radio Bursts with Their Host Galaxies.
188 *Astrophys. J.* **849**, 162 (2017). 1705.02998.
- 189 14. Suzuki, R. et al. Multi-Object Infrared Camera and Spectrograph (MOIRCS) for the Subaru
190 Telescope I. Imaging. *PASJ* **60**, 1347 (2008).
- 191 15. Brinchmann, J. et al. The physical properties of star-forming galaxies in the low-redshift
192 Universe. *Mon. Not. R. Astron. Soc.* **351**, 1151–1179 (2004). astro-ph/0311060.
- 193 16. Ioka, K. The Cosmic Dispersion Measure from Gamma-Ray Burst Afterglows: Probing the
194 Reionization History and the Burst Environment. *Astrophys. J. Lett.* **598**, L79–L82 (2003).
195 astro-ph/0309200.

- 196 17. Cordes, J. M. & Lazio, T. J. W. NE2001.I. A New Model for the Galactic Distribution of Free
197 Electrons and its Fluctuations. arXiv e-prints astro-ph/0207156 (2002). [astro-ph/0207156](#).
- 198 18. Spitler, L. G. et al. A repeating fast radio burst. *Nature* **531**, 202–205 (2016). [1603.00581](#).
- 199 19. Chime/Frb Collabortion. Recent high activity from a repeating Fast Radio Burst discovered
200 by CHIME/FRB. The Astronomer’s Telegram **14497**, 1 (2021).
- 201 20. Day, C. K., Bhandari, S., Deller, A. T., Shannon, R. M. & Moss, V. A. ASKAP localisation of
202 the FRB 20201124A source. The Astronomer’s Telegram **14515**, 1 (2021).
- 203 21. Ricci, R. et al. Detection of a persistent radio source at the location of FRB20201124A with
204 VLA. The Astronomer’s Telegram **14549**, 1 (2021).
- 205 22. Ravi, V. et al. The host galaxy and persistent radio counterpart of FRB 20201124A.
206 arXiv e-prints arXiv:2106.09710 (2021). [2106.09710](#).
- 207 23. Pleunis, Z. et al. Fast Radio Burst Morphology in the First CHIME/FRB Catalog.
208 arXiv e-prints arXiv:2106.04356 (2021). [2106.04356](#).
- 209 24. Connor, L., Miller, M. C. & Gardenier, D. W. Beaming as an explanation of the repeti-
210 tion/width relation in FRBs. *Mon. Not. R. Astron. Soc.* **497**, 3076–3082 (2020). [2003.11930](#).
- 211 25. Heintz, K. E. et al. Host Galaxy Properties and Offset Distributions of Fast Radio Bursts:
212 Implications for Their Progenitors. *Astrophys. J.* **903**, 152 (2020). [2009.10747](#).
- 213 26. Bhardwaj, M. et al. A Nearby Repeating Fast Radio Burst in the Direction of M81.
214 Astrophys. J. Lett. **910**, L18 (2021). [2103.01295](#).

- 215 27. Li, D. et al. A bimodal burst energy distribution of a repeating fast radio burst source.
216 arXiv e-prints arXiv:2107.08205 (2021). 2107.08205.
- 217 28. Margalit, B. & Metzger, B. D. A Concordance Picture of FRB 121102 as a Flaring Magnetar
218 Embedded in a Magnetized Ion-Electron Wind Nebula. *Astrophys. J. Lett.* **868**, L4 (2018).
219 1808.09969.
- 220 29. Murase, K., Kashiyama, K. & Mészáros, P. A burst in a wind bubble and the impact on
221 baryonic ejecta: high-energy gamma-ray flashes and afterglows from fast radio bursts and
222 pulsar-driven supernova remnants. *Mon. Not. R. Astron. Soc.* **461**, 1498–1511 (2016). 1603.
223 08875.
- 224 30. Piro, A. L. & Gaensler, B. M. The Dispersion and Rotation Measure of Supernova Remnants
225 and Magnetized Stellar Winds: Application to Fast Radio Bursts. *Astrophys. J.* **861**, 150
226 (2018). 1804.01104.
- 227 31. Chatterjee, S. Fast radio bursts. *Astronomy and Geophysics* **62**, 1.29–1.35 (2021).

228 **Correspondence and requests for materials** These should be addressed to Di Li (dili@nao.cas.cn).

229 **Acknowledgements** This work was supported by the Cultivation Project for FAST Scientific Payoff and
230 Research Achievement of CAMS-CAS and also supported by National Natural Science Foundation of China
231 (NSFC) Programs No. 11988101, No. 11725313, No. 11690024, No.12041303 No. U1731238, No.
232 U2031117, No. U1831131, No. U1831207; CHN acknowledges support from the FAST Fellowship. SC,
233 JMC, and SKO acknowledge support from the National Science Foundation (AAG 1815242) and are mem-

234 bers of the NANOGrav Physics Frontiers Center, which is supported by NSF award PHY-1430284. CJL
235 acknowledges support from the National Science Foundation under Grant No. 2022546. KA, SBS and
236 RAT acknowledges support from NSF grant AAG-1714897. PW thanks the YSBR-006, CAS Project for
237 Young Scientists in Basic Research. SBS is a CIFAR Azrieli Global Scholar in the Gravity and the Ex-
238 treme Universe program. YN acknowledges support from JSPS KAKENHI Grant Number JP20H01942.
239 JJ acknowledges support from the Japan Society for the Promotion of Science (JSPS) KAKENHI grant
240 JP19K23456 and JP18J12714. SD is the recipient of an Australian Research Council Discovery Early Ca-
241 reer Award (DE210101738) funded by the Australian Government. We thank the FAST key science project
242 for supporting follow-up observations. We also thanks the FAST collaborations and realfast team for the
243 technical support. Some data presented herein were obtained at the W. M. Keck Observatory, which is op-
244 erated as a scientific partnership among the California Institute of Technology, the University of California
245 and the National Aeronautics and Space Administration. The Observatory was made possible by the gen-
246 erous financial support of the W. M. Keck Foundation. This study is based in part on data collected at the
247 Subaru Telescope, which is operated by the National Astronomical Observatory of Japan. The National
248 Radio Astronomy Observatory is a facility of the National Science Foundation operated under cooperative
249 agreement by Associated Universities, Inc.

250 **Author contributions** CHN discovered the source FRB190520. DL, CL, SC, CWT, WY, CHN initiated
251 the follow-up projects. DL, CHN, BZ, WWZ led the follow-up FAST observations. CHN, JMY, YKZ,
252 PW, DJZ, YF searched and processed the FAST data. WY is the PI of the VLA observations and requested
253 simultaneous FAST and Swift ToO observations. KA, CL, SC, XZ, SBS, ZY, WY, LC contributed to the
254 VLA burst detection and localization, identification and measurements of the associated PRS. CWT, SC,
255 DS, YN, JJ, CB, GDL contributed to the Optical/NIR follow-up observations, host galaxy photometry,

256 morphology, and spectroscopic analysis. ZY and WY contributed to the Swift data analysis. SO, JMC, SC,
257 JMY, CHN contributed to measured the burst scattering, modeling combined with analysis of propagation
258 effects and DM-z analysis. JMC, BZ and WYW contributed to the DM_{host} estimation. KA, YKZ, JRN,
259 RL, WWZ, CHN, contributed to the signal period and burst rate analysis. PW, YKZ helped on Energy
260 calibration and MY contributed to the RFI removal on FAST data. MC led the Effelsberg follow-up, SD led
261 the Parks observations, and YLY led the FAST-VLBI experiment. SBS, DL, KA, CHN, SC, and CL had
262 major contributions to the preparation of the manuscript. All of the authors have reviewed, discussed, and
263 commented on the present results and the manuscript.

264 **Competing financial interests** The authors declare that they have no competing financial interests.

265 **Methods**

266 **1 Observations**

267 **FAST CRAFTS** is a multi-purpose drift scan survey conducted with FAST using a 19-beam re-
268 ceiver operating at 1.05–1.45 GHz, deployed in May 2018 and conducting blind FRB searches
269 using multiple pipelines³¹. FRB 190520 was discovered on November 16th 2019 in archived
270 CRAFTS data which is in 1-bit filterbank format with $196 \mu\text{s}$ time resolution and 0.122 MHz
271 frequency resolution. In this first discovery observation, 3 bursts were detected in 10 seconds, and
272 another burst was detected 20 seconds later. These 4 bursts from the drift scan survey gave a pre-
273 liminary location for the source within a ~ 5 arcmin diameter region. Taking the pointing location
274 from FAST, 2 follow-up observations were performed with FAST on April 25th and May 22nd
275 in 19-beam mode in which 15 bursts were detected. A monthly observation campaign was then
276 conducted by FAST using the ~ 100 mas localization from VLA. After some regular telescope
277 maintenance, 10 observations were performed spanning from July 30th 2020 to September 19th
278 2020 in which 60 more bursts were detected.

279 Bursts were detected from FRB 190520 in each FAST monitor observation. We list the
280 properties of those bursts detected by FAST in Table 1 . The burst arrival time is in MJD format
281 and has been transformed to the arrival time at the solar system barycentre (SSB) at 1.5GHz. We
282 estimate the structure maximizing DM³² for the brightest burst from each day, and report the same
283 DM (DM_b) for all other bursts detected in that observation. The pulse widths were estimated by a
284 Gaussian profile fit if the burst showed no obvious sign of scattering. The sub-pulse is recognized

285 if the profile peak does not fall behind the noise baseline. If the burst shows a scattering tail
286 (see Section 5), the pulse width is derived from the scatter tail fit. The bandwidth of each burst
287 is roughly estimated by its spectrum after the Radio Frequency Interference (RFI) elimination.
288 A 1-Kelvin equivalent noise calibration signal was injected before each observation session to
289 obtain high quality flux density and energy calibration measurement for each detected burst. The
290 injected noise calibration signal was used to scale the data noise level of the baseline to the system
291 temperature (T_{sys}) units, the standard deviation of off-pulse brightness is nearly constant within
292 6% for all observations. The variation in the off-pulsed noise level mainly comes from the zenith
293 angle dependent telescope gain. The Kelvin unit was then converted to Jy using the zenith angle-
294 dependent gain curve, provided by the observatory through quasar measurements³³. For most
295 observations, the zenith angle was less than 20 degrees, which corresponds to a stable gain of ~ 16
296 K/Jy. The zenith angle-dependent gains were then applied to the amount of pulsed flux above the
297 baseline, giving the peak flux measurement of the detected bursts.

298 The FAST observation data was searched using a Heimdall based pipeline^{31,34}. For the
299 FRB blind search in 19-beams drift scan survey, the polarizations were merged and only kept
300 stokes I, the trial DM range is from 100 to 5000 pc cm^{-3} and the pulse width is adapted by a box
301 car in the search. The candidates above a S/N of 7 and present in less than 4 adjacent beams were
302 manually examined for further inspection. After we identified FRB 190520 as a new FRB source,
303 the follow-up burst search was taken with narrower DM range (100-2000 pc cm^{-3}). Following the
304 VLA localization, the tracking observation only recorded data from central beam but with all the
305 stokes parameters and higher time resolution (49.98 μs). Candidates with S/N > 7 sigma correspond

306 to a fluence threshold of 9 mJy ms.

307 **VLA** Following the FAST detection of bursts from FRB 190520 and its high burst rate, VLA
308 observations were performed from July-October 2020 at the most reliable position determined
309 using FAST detections. At the time of proposing, the location of this FRB was constrained to
310 within 5 arcmin using multiple burst detections at FAST. The observations were done under the
311 approved DDT project: 20A-557 and were performed at L, S and C bands. In total, 11.4 hrs were
312 spent on the source. Most of the observations were in the B array configuration (with a maximum
313 baseline of 11.1 km), with the exceptions that the array configuration was BnA on MJD 59161 and
314 BnA->A on MJD 59167 and 59169. The total bandwidths at L (1.5 GHz), S (3 GHz), and C (5.5
315 GHz) bands were 1024, 2022 and 2022 MHz, respectively, with 1024 channels, corresponding to
316 channel band-widths of approximately 1, 2 and 2 MHz.

317 The details of the observations are given in Table 2 . The telescopes were pointed at the field
318 centered at (RA, Dec)[J2000] = (16h02m01s, -11d17m28s). We note that due to a system error
319 the *realfast* system wasn't run on the VLA observation on MJD 59169. However, this observation
320 was used to make a deep radio image at S band.

321 We used the *realfast* search system at VLA to search for bursts from FRB 190520 in our
322 VLA observations. The *realfast* search system has been described in detail in ^{11,35}, but here we
323 discuss it briefly. Using a commensal correlator mode, the visibilities are sampled with 10 ms
324 resolution and distributed to the *realfast* GPU cluster for transient search. The search pipeline
325 *rfpipe* ³⁶ then applies the online calibration, de-disperses the visibilities and forms images at

326 varying temporal widths. The 8σ fluence limit of a 10 ms image is 0.4 Jy ms. Candidates with
327 image S/N greater than the threshold triggered the recording of fast sampled visibilities around 2-5
328 seconds of the candidate. Each candidate is then post-processed, and classified by `fetch`, a GPU
329 based convolutional neural network to classify radio transients from non-astrophysical signals ³⁷.
330 Interesting candidates are then visually checked by the *realfast* team and marked for further offline
331 analysis.

332 Promising candidates selected by the *realfast* team goes through an offline analysis to refine
333 the parameters of the candidate, and improve its detection significance, if possible. Several meth-
334 ods are tried within this analysis: offline search for the transient using a finer DM grid, varying
335 RFI flagging parameters, changing image size (as realtime-search is done on non-optimal image
336 size due to computational limitations), sub-band search etc (see section 2.4 of ³⁵ for more details).
337 Significance of an astrophysical transient should improve when the data is de-dispersed at a DM
338 closer to the DM of the candidate (see section 2 of ³⁸). Noise like events or RFI are sensitive to
339 RFI flagging and image gridding parameters, and so they cannot be reproduced on refinement, and
340 are discarded. Sometimes the transient signal is present only in a subband out of the whole band-
341 width, so we also rerun our search only using the relevant frequencies, which further improves the
342 detection significance. We applied all these techniques on all the interesting candidates from these
343 observations, and used those refined parameters further in the analysis.

344 **2 Localization of bursts**

345 **Calibration** The images generated by the real-time system make several assumptions during cal-
346 ibration and imaging. This is to improve the computational efficiency and perform the imaging
347 and search in real-time. Moreover, the Point Spread Function (PSF) of the interferometer is not
348 deconvolved from the image, so the real-time system forms “dirty” images. This does not opti-
349 mally concentrate the signal of a point source to a small region, but it spreads it over the PSF of
350 the telescope.

351 To address these issues, we used the raw, de-dispersed, fast sampled visibilities with just the
352 burst signal to re-image the burst data with Common Astronomy Software Application package
353 (CASA v5.6.2-3)³⁹. We first downloaded the VLA calibration pipeline tables corresponding to
354 each observation with the burst. We then applied those calibration and flagging tables to the burst
355 data using CASA task `applycal`. Observation of 3C 286 (before the FRB observation) was used
356 to calibrate the flux density scale, bandpass and delays. Complex gain fluctuations over time were
357 calibrated with observations of calibrator J1558-1409.

358 **Determining properties of individual bursts** After calibration, we used the CASA task `tclean`
359 to generate the image and estimate an image Signal to Noise (S/N). For each burst, we search dif-
360 ferent spectral window ranges to generate the image with highest S/N. This is because most of the
361 bursts are frequency modulated, and therefore selecting a sub-band would improve the detection
362 significance. We then use the CASA task `imfit` around the rough FRB position to fit an ellipse to
363 the source in the radio image and measure the centroid location, peak flux density and 1σ uncer-

364 tainties. We then take the weighted average of all burst positions, by weighing each position by the
365 inverse of the position fit errors reported by CASA. This weighting scheme accounts for the effects
366 of different beam size at different frequencies along with different significance of detection. This
367 is because fit errors are inversely proportional to signal to noise ratio, and therefore high signifi-
368 cance detection is expected to have smaller fit errors. Moreover, a high frequency detection would
369 have smaller beam size, again leading to a smaller fit error. We observe both these effects as per
370 our expectation in our fits. Using this, we obtained the best estimate for burst position of: R.A.=
371 16h02m04.2683s, Decl.= -11d17m17.3203s (J2000). We estimate statistical error to be 0.023'' and
372 0.042''.

373 We use BURSTFIT to model the spectro-temporal properties of bursts. This analysis extends
374 the discussion of ⁴⁰ and has been described in ⁴¹. We model the pulse profile and the spectra using
375 a Gaussian function, and therefore fit for 6 parameters: mean of pulse, width of pulse, mean of
376 spectra, width of spectra, fluence and DM. Following ⁴¹, we use CURVE_FIT followed by MCMC
377 methods to estimate the posterior distribution of these fit parameters. The fitted properties of the
378 VLA bursts are given in Table 5 . Burst S5 was very weak, and hence its fit estimates are not well
379 constrained. Burst times are defined in barycentric MJD time that are referenced to the frequency
380 at the top of the receiver band referenced in the burst name. For bursts in L, S, and C bands, the
381 reference frequencies are 2032, 4012, and 6512 MHz, respectively.

382 **3 Persistent Radio Source**

383 **Deep radio images and PRS** The VLA visibilities with 3 or 5 s sampling time were saved and an-
384 alyzed to search for persistent radio emission. We used standard data reduction, including flagging
385 and calibration with the CASA software package³⁹. We used 3C 286 as the primary calibrator for
386 flux scaling and bandpass calibration. J1558-1409 was used as secondary calibrator to calibrate
387 the complex gains as a function of time. We then performed further flagging on the target and then
388 subsequently imaged its Stokes I using the CASA deconvolution algorithm `tclean`. To balance
389 sensitivity while reducing sidelobes from a nearby bright source, we imaged with a Briggs weigh-
390 ing scheme (`robust=0`). In addition, self-calibrations were performed for all observations to correct
391 considerable artefacts from the close-by bright sources in the field. We made use of the CASA task
392 `imfit` to measure source flux densities by fitting a point source with an elliptical Gaussian model
393 with the size and shape of the restoring beam in the image plane.

394 The VLA campaign obtained two-epochs at 1.5 GHz, six-epochs at 3 GHz and 5.5 GHz,
395 which resulted in an on-source time of ~ 3 hours for 1.5 GHz, ~ 4 hours for both 3 GHz and
396 5.5 GHz. We stacked observations at each central frequency in the uv-plane and then imaged the
397 Stokes I intensity, resulting in 1.5 GHz, 3 GHz, and 5.5 GHz deep images with rms noise of 9.0,
398 4.5, and 3.0 $\mu\text{Jy}/\text{beam}$, respectively. The obtained positions for the PRS are shown in Table 3 . The
399 systematic offsets on these positions are estimated in the next section.

400 **Systematic Offsets** In order to determine the systematic errors on the coordinates of the PRS
401 that we determined from the deep images, we ran PyBDSF (<https://www.astron.nl/citt/>

402 pybdsf/index.html) package to extract radio sources from the deep images. We then cross-
403 matched the detected point sources in the deep images with the sources listed in the optical
404 PanSTARRS survey DR1 ⁴². We identified the radio point sources using the following criteria:

- 405 • The peak intensity (Jy/beam) of a source should be 0.7, 0.5, 0.5 times higher than its inte-
406 grated flux (Jy) for the 1.5 GHz, 3 GHz and 5.5 GHz images, respectively.
- 407 • The S/N (peak intensity / local rms noise) of a source should be greater than 5.

408 In total, we detected 375, 113, and 43 sources in the 1.5 GHz, 3 GHz and 5.5 GHz deep
409 image, respectively. We visually checked the selected sources to make sure that they are ‘point-
410 like’ sources in the deep images. Of those, 109, 27, and 9 sources had an optical source within
411 0.5 arcsec in the PanSTARRS DR1 catalogue. By comparing the offsets of these cross-matched
412 sources, we estimate the systematic offsets in our 1.5 GHz, 3 GHz and 5.5 GHz positions. They are
413 listed in Table 3 . The errors on the systematic offsets are consistent with zero and the uncertainty
414 in that offset dominates the uncertainties of the position of the PRS. We report the PRS coordinates
415 based on the measurements at 3 GHz, which has the smallest errors on the systemic offsets.

416 **Variability and Spectrum of the PRS** The flux density of the source measured in each epoch is
417 shown in Table 2 . In order to study the spectrum of the PRS, we split each of the observations into
418 two, 1 GHz sub-bands. Then we measured the average flux density at each of the sub-bands over
419 the campaign. By applying a Power-Law(PL) model to fit the multi-band data, we determined the
420 average PL spectral index of the PRS as -0.41 ± 0.04 . This is shown in Figure 3 .

421 **Chance of coincident association of the PRS** In the 1.5 GHz deep image, We detected 8 ‘point-
422 like’ sources , including the PRS (based on our point-source selection criteria described earlier),
423 with a flux density higher than $260 \mu\text{Jy}$ within 5 arcminutes of the phase center. There is an
424 additional bright source with a flux density of a few tens mJy in the region, but it was not classified
425 as a ‘point-like’ source based on our criteria.

426 To estimate the chance coincidence probability of the PRS with the bursts, we compared
427 the solid angle corresponding to the uncertainty of burst localization and the average solid angle
428 occupied by each of the eight ‘point-like’ sources in the FRB field-of-view. The solid angle corre-
429 sponding to each of the 8 ‘point-like’ sources is roughly estimated as $S_{\text{source}} = \pi(5/60)^2/8$ Sr. The
430 offset between the average position of the nine bursts and the position of the PRS at 3 GHz, which
431 is best constrained when taking both statistical and systematic errors into account, is about 0.13
432 arcseconds. This, along with a statistical error of 0.02 arcseconds and a conservative estimate of
433 the systematic error of 0.1 arcseconds, can be used to estimate the offset between the PRS and the
434 FRB position. We conservatively estimate this offset to be 0.25 arcseconds. The solid angle corre-
435 sponding to the offset therefore can be estimated as $S_{\text{offset}} = \pi \times (0.25/60/60)^2$ Sr. The ratio between
436 S_{offset} and S_{source} gives the chance of coincident association of the PRS with the FRB position to be
437 $\approx 6 \times 10^{-6}$.

438 **4 Optical Redshift Determination**

439 The deep R' -band ($5427\text{\AA} - 7041\text{\AA}$) images obtained by CFHT/MegaCam are stacked from archival
440 observation data taken in 2014-2015 by the CFHT archival pipeline MEGAPIPE, with a total \sim

441 3.6 hours on the field. The level 3 (flux calibrated) images are retrieved for our analysis.

442 NIR J -band images of FRB 190520 field were taken under a relatively poor seeing condition
443 ($\sim 1.3''$) through the Subaru ToO observation on August 05th 2020. A total of 1.4-hour obser-
444 vations were used for the final combined J -band image shown in Figure 2. A J -band blob of
445 22.07 ± 0.14 mag (AB) was detected at $\sim 1''$ south east of the burst location, possibly the stellar
446 emission of the host galaxy. A faint northern blob at $2.5''$ north has 22.87 ± 0.26 mag in J -band.
447 None of these two sources are detected in Ks -band image, with a 5-sigma limit of 21.74 mag (1.1
448 hours).

449 An optical spectrum was obtained with Double Spectrograph (DBSP) on the Palomar 200-
450 inch telescope on 24th July 2020 using a $1''$ slit-width. This observation was executed before the
451 CFHT archival MegaCAM data on FRB 190520 field were found, and only Pan-STARRS images
452 were used for observation planning. The slit of DBSP was set to cover the FRB optical counterpart
453 located at the VLA persistent radio source emission in L-band observed on 22nd July 2020 at
454 RA = 16:02:04.27; Dec. = $-11:17:17.5$ which later is found to coincide with the location of the
455 pulsation emission from FRB 190520 in $0.18''$. No clear optical counterpart was detected in any
456 of the 5 band images of PanSTARRS from DR1 ⁴². The slit was guided by the nearby M-star
457 at RA = 16:02:04.48, Dec. = $-11:17:19.1$ as reported in PanSTARRS DR1 catalog, with $i =$
458 20.4 mag, and due east of $3.4''$ away from the coordinate of the VLA PRS. The slit was set to
459 a position angle of 108.5 degrees, allowing both the coordinate of VLA persistent radio source
460 and the M-star to fall in to the slit. The observations with 2×900 s exposures were carried out
461 under photometric sky condition and sub-arcsecond seeing. The 2D spectrum was generated in

462 IRAF, including bias removal, flat-fielding, and reduction on other instrumentation effects. The
 463 1D spectrum was extracted from a 1.5'' window. The standard star BD+28 4211 is used for telluric
 464 correction and flux calibration. The DBSP 1-D spectrum is shown in Figure 4 . The flux scale of
 465 the spectrum does not include the slit loss and registration error of Pan-STARRS coordinates of the
 466 M-type star. The [OIII] 5007Å line and the H α line are both well detected ($> 5\sigma$). Two emission
 467 lines are narrow, with a FWHM of $\sim 10\text{\AA}$. The corresponding redshift derived based on these two
 468 spectral lines is $z = 0.241$.

469 A follow-up Keck LRIS spectroscopic observation was carried out on 25th August 2020
 470 under reasonable weather and seeing conditions (1.1'') . The 1.5'' slit was set at a position angle of
 471 160° to the extended optical emission seen in the MegaCam *R*-band image around the FRB 190520
 472 location. A total exposure of 3600 s was obtained. The emission lines H α , H- β , [OIII]4859A, and
 473 [OIII]5007A are well detected, indicating the extended *R'*-band structure has the same redshift of
 474 $z = 0.241$.

475 5 FAST Burst Sample Analysis

476 **Repetition rate** FRB 190520 is very active and bursts from it were detected in each monitoring
 477 observation with FAST. Because of the possible clustering behavior of FRB emission, a Weibull
 478 distribution

$$W = \frac{k}{\lambda} \left(\frac{\delta}{\lambda} \right)^{k-1} e^{-(\delta/\lambda)^k} \quad (1)$$

479 is used to describe the distribution of waiting time⁴³, where δ is the waiting time and k is the
 480 shape parameter. The Weibull distribution reduces to the Poissonian case when $k = 1$, and $r =$

481 $1/[\lambda\Gamma(1 + 1/k)]$ indicates the burst rate of the FRB emission. Figure 5 shows the result of the
482 parameters distribution obtained with Markov Chain Monte Carlo (MCMC). We find the burst rate
483 of FRB 190520 is $r = 4.5^{+1.9}_{-1.5} \text{ hr}^{-1}$ with shape parameters $k = 0.37^{+0.04}_{-0.04}$ for all 79 bursts which
484 are above $7\sigma > 9.3 \text{ mJy} \cdot \text{ms}$ (left panel in Figure 5), and $r = 5.3^{+1.1}_{-1.0} \text{ hr}^{-1}$ with shape parameters
485 $k = 0.76^{+0.09}_{-0.08}$ for excluding waiting time shorter than 1 s (right panel in Figure 5).

486 **Short and long time scale periodicity search** A period search was conducted from the total
487 75 bursts from FAST. We searched for periodicity in the times of arrival for FRB 190520 using
488 the phase-folding method. The phases of all the pulses were calculated in the parameter space
489 composed by period (P) and period derivative (\dot{P}). For the short time scale periodicity, the pulses
490 are aligned according to the arrival time of the first burst in each observing session. Then we
491 collected the contiguous inactivity fraction by traversing the period (P) among $10^{-3} - 10^3 \text{ s}$ and
492 period derivative (\dot{P}) among $10^{-12} - 10^0 \text{ s s}^{-1}$. Almost all values in this figure are less than 0.4.
493 This indicates that no obvious period between 1 ms and 1000s was detected in FRB 190520.

494 For a long time scale period, we folded all the pulses in the range of period (P) among
495 $2 - 365 \text{ d}$ and period derivative (\dot{P}) among $10^{-12} - 10^0 \text{ d d}^{-1}$. 169 d and 67 d seem to be the
496 possible periods. We then folded all the mjds of each observation session in the same period (P)
497 and period derivative (\dot{P}) range. The structure of the contiguous inactivity fraction around 169 d
498 and 67 d is similar for the observing session mjds and the arrival times of detected pulses, which
499 indicates that the 169 d and 67 d are caused by the selection effect of observations. Thus, no long
500 or short period of FRB 190520 was detected.

501 **DM analysis** The observed DM_{obs} can be separated into four primary components:

$$DM_{\text{obs}} = DM_{\text{MW}} + DM_{\text{halo}} + DM_{\text{IGM}} + DM_{\text{host}}, \quad (2)$$

502 where DM_{MW} is the contribution from our Galactic interstellar matter, DM_{halo} is the contribution
 503 from the Milky Way halo, DM_{host} the contribution from the host galaxy including its halo and
 504 any gas local to the FRB source, and DM_{IGM} is the contribution from the intergalactic medium.
 505 The value of DM_{MW} is estimated from Galactic electron density models, in which $DM_{\text{MW}} =$
 506 60.21 pc cm^{-3} from the NE2001 model¹⁷ and $DM_{\text{MW}} = 50.23 \text{ pc cm}^{-3}$ from the YMW16 model
 507⁴⁴. The DM associated with the Milky Way halo is allowed to range from 25 to 80 pc cm^{-3} .
 508 With the assumption of Λ CDM cosmological model and using the host galaxy's redshift of 0.241,
 509 the value of DM_{IGM} is approximately $200_{-65}^{+107} \text{ pc cm}^{-3}$ where we have adopted a baryon fraction
 510 $f_{\text{IGM}} = 0.8$ for the ionized IGM based on discussion in⁴⁵ and the range represents cosmic variance
 511 in DM_{IGM} but does not include uncertainty in f_{IGM} . The mean value is given by⁴⁶

$$DM_{\text{IGM}} = \frac{3cH_0\Omega_b f_{\text{IGM}}}{8\pi Gm_p} \int_0^z \frac{\chi(z)(1+z)dz}{[\Omega_m(1+z)^3 + \Omega_\Lambda]^{\frac{1}{2}}}, \quad (3)$$

512 where the free electron number per baryon in the universe is $\chi(z) \approx 7/8$, $\Omega_m = 0.315 \pm 0.007$, $\Omega_b h^2 =$
 513 0.02237 ± 0.00015 , and $H_0 = 67.36 \pm 0.54 \text{ km s}^{-1} \text{ Mpc}^{-1}$ ⁴⁷. The averaged DM_{obs} from all bursts
 514 is $1202 \pm 10 \text{ pc cm}^{-3}$, thus we could regard the averaged DM_{host} as $906 \pm 10 \text{ pc cm}^{-3}$ and 921.1 ± 10
 515 pc cm^{-3} for NE2001 and YMW16 model separately.

516 The DM of the host galaxy is independently estimated from its $H\alpha$ emission by converting
 517 the extinction-corrected $H\alpha$ flux, $F_{H\alpha} = (9.4 \pm 0.3) \times 10^{-16} \text{ erg s}^{-1} \text{ cm}^{-2}$, to an $H\alpha$ surface density
 518 of $503 \pm 14 \text{ Rayleighs}$ in the source frame at $z = 0.241$, assuming host galaxy dimensions of 0.5 by

519 0.5 arcseconds⁴⁸. The H α surface density $S(\text{H}\alpha)$ is related to the emission measure (EM) in the
 520 source frame by

$$\text{EM}_s = 2.75 \text{ pc cm}^{-6} (1+z)^4 T_4^{0.9} S(\text{H}\alpha) \approx 1383 \pm 17 \text{ pc cm}^{-6} \times T_4^{0.9} \left[\frac{S(\text{H}\alpha)}{503 \pm 14 \text{ R}} \right], \quad (4)$$

521 where we have used the redshift $z = 0.241$. Then, using the relation $\text{EM} = [\zeta(1 + \epsilon^2)/f]\text{DM}^2/L$
 522 we obtain the corresponding source frame DM,

$$\text{DM}_s \approx 588 \pm 8 \text{ pc cm}^{-3} \times T_4^{0.45} \left(\frac{L}{5 \text{ kpc}} \right)^{1/2} \left[\frac{f/0.1}{\zeta(1 + \epsilon^2)/2} \right]^{1/2} \left[\frac{S(\text{H}\alpha)}{212 \pm 6 \text{ R}} \right]^{1/2}, \quad (5)$$

523 where we have adopted fiducial values of $f = 0.1$, $\zeta = \epsilon = 1$, $L = 5 \text{ kpc}$. In the observer's
 524 frame, the measured DM contribution of the host galaxy is smaller by a factor of $1/(1+z)$, yielding
 525 $\text{DM}_{\text{h,coeff}} \sim 474 \pm 7 \text{ pc cm}^{-3}$ for the coefficient. To match the inferred value of $\text{DM}_h \sim 900 \text{ pc cm}^{-3}$
 526 requires that the three factors in Eq. 5 involving T_4 , L and f combine to a factor $\simeq 2$. A factor of
 527 five higher temperature, $T_4 \simeq 5$, could accomplish this, for example. However, the temperature
 528 would need to be even larger because the path length sampled by the FRB through the host galaxy
 529 could be smaller depending on its location relative to the H α emitting region, while other factors
 530 (ζ , ϵ and f) could alter the required temperature still more depending on the local properties of the
 531 gas. We note that the quoted errors only account for measurement errors in the H α flux.

532 **Prominent scintillation and scattering** Most of the pulses of FRB 190520 show scintillation-
 533 induced variation of intensity with frequency. This kind of variation is always quantified by a
 534 de-correlation bandwidth, $\Delta\nu_d$. To estimate $\Delta\nu_d$, we formed 1D auto-correlation functions (ACFs)
 535 of the pulse intensity variation. The 1D ACF can be described by³,

$$I(\Delta\nu) = \frac{m}{\Delta\nu_d^2 + \Delta\nu^2} \quad (6)$$

536 where $\Delta\nu$ is the frequency lags. Using Equation 6 to fit the peak of the ACF, we get the $\Delta\nu_d$ of each
537 burst. We find the averaged $\Delta\nu_d$ is 0.3 ± 0.13 MHz.

538 For FRB 190520, the DM contributed by the Galactic disk is 50.23 pc cm^{-3} predicted by
539 YMW16⁴⁴. Based on the relation between the Galactic DM and scattering timescale⁴⁴, we find
540 that the corresponding Galactic scattering timescale at 1.4 GHz yields a scintillation bandwidth of
541 0.46 MHz, which is comparable with the observed average value 0.3 ± 0.13 MHz at 1.4 GHz.

542 Among the detected 79 pulses of FRB 190520, 28 pulses show frequency-dependent tempo-
543 ral width that is consistent with scattering. To measure the pulse width and scattering timescale
544 of FRB 190520, using the dynamic spectra, we first fold the frequency and normalized the pulse
545 profile. And then, for pulses with scattering tail we use a Gaussian component convolved with a
546 one-sided exponential component to fit the pulse profile, and use a single Gaussian component to
547 fit the rest. The upper panels of Figure 1 show histograms of the distributions for the scattering
548 timescales at 1.25 GHz and the pulse width. The histograms can be roughly described by a Gaus-
549 sian function with peaks at 10.8 ± 0.5 ms and 12.5 ± 0.7 ms for scattering timescale and pulse width,
550 respectively.

551 The observed mean scattering time of 10.8 ms at 1.25 GHz is far too small for the FRB's
552 host galaxy to lie behind our proposed host galaxy association. In this alternative scenario, the
553 host galaxy would lie at a redshift $z_h \sim 0.5$, the redshift implied by the DM- z relation with a
554 foreground galaxy DM contribution of about 474 pc cm^{-3} based on H α EM. The FRB would pass
555 through an intervening galaxy at a redshift $z_l = 0.241$ at an impact parameter of about 4 kpc. The

556 scattering contribution of the intervening galaxy lens is related to its DM contribution by⁴⁹

$$\tau(\text{DM}, \nu, z) \approx 48.03 \mu\text{s} \times \frac{\tilde{F} G \text{DM}_l^2}{(1 + z_l)^3 \nu^4}, \quad (7)$$

557 where DM_l is the DM contribution of the lens galaxy in pc cm^{-3} in the lens frame, ν is the observing
 558 frequency in GHz, z is the lens galaxy redshift, and $\tilde{F} = \zeta \epsilon^2 / f (l_0^2 l_i)^{1/3}$ quantifies the electron density
 559 fluctuations in the lens for \tilde{F} in units of $\text{pc}^{-2/3} \text{ km}^{-1/3}$. The geometric factor G is unity for scattering
 560 in a host galaxy but it can be very large for an intervening galaxy, in which case $G \approx d_{\text{sl}} d_{\text{lo}} / d_{\text{so}} L$,
 561 where d_{sl} , d_{lo} , and d_{so} are the angular diameter distances between the source and lens, lens and
 562 observer, and source and observer, respectively, and L is the path length through the lens. Adopting
 563 the DM implied by the $\text{H}\alpha$ emission (see above) and $\tilde{F} \approx 0.1 \text{ pc}^{-2/3} \text{ km}^{-1/3}$, characteristic of a
 564 source embedded in a galaxy disk⁴⁹, we find $\tau \approx 3 \text{ s}$ at 1.25 GHz. For the FRB to be located
 565 in a background galaxy and have the observed scattering, the DM contribution of the intervening
 566 galaxy would have to be less than about 100 pc cm^{-3} , which would require a significantly smaller
 567 path length through the galaxy, significantly larger value of ζ , or a significantly smaller filling
 568 factor f .

569 **Rotation measure** Rotation measure (RM) is searched at L-band with FAST data. The polariza-
 570 tion was calibrated by correcting for differential gains and phases between the receptors through
 571 separate measurements of a noise diode injected at an angle of 45° from the linear receptors. We
 572 searched for the rotation measure (RM) from -3.0×10^5 to $3.0 \times 10^5 \text{ rad m}^{-2}$. No significant peak
 573 was found in the Faraday spectrum. We estimate the depolarization fraction f_{depol} using Equation

574 8

$$f_{\text{depol}} = 1 - \frac{\sin(2\Delta\theta)}{2\Delta\theta}, \quad (8)$$

575 where the intra-channel Faraday rotation $\Delta\theta$ is given by

$$\Delta\theta = \frac{RMc^2\Delta\nu}{\nu_c^3}, \quad (9)$$

576 where c is the speed of light, $\Delta\nu$ is the channel width, and ν_c is the central channel observing
577 frequency. Taking $\Delta\theta = 1$ rad, $\Delta\nu = 0.122$ MHz, and $\nu_c = 1.25$ GHz for our data, we get $RM =$

578 1.8×10^5 rad m⁻² and depolarization fraction of 54.5% caused by intra-channel Faraday rotation.

579 Assuming that the pulse is 100% linearly polarized intrinsically and the non-detection of RM is

580 caused by intra-channel Faraday rotation, we place an lower limit on the RM of 1.8×10^5 rad m⁻².

581 Such a large RM is even larger than that of FRB 121102⁵⁰, which suggests that FRB 190520 also

582 resides in an extreme magneto-ionic environment. Large RM also indicates that the FRB 121102

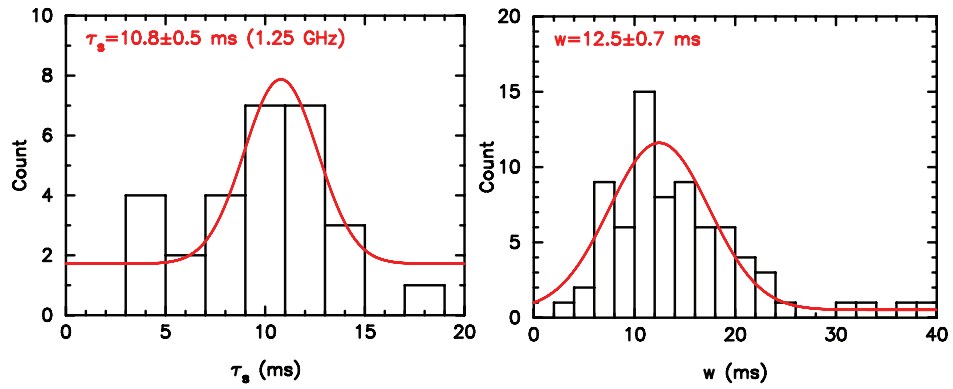
583 could be very young^{30,51}, similarly, FRB 190520 could also be very young.

- 585 31. Niu, C.-H. et al. CRAFTS for fast radio bursts: Extending the dispersion–fluence relation with
586 new FRBs detected by FAST. The Astrophysical Journal Letters **909**, L8 (2021).
- 587 32. Hessels, J. W. T. et al. FRB 121102 Bursts Show Complex Time-Frequency Structure.
588 Astrophys. J. Lett. **876**, L23 (2019). 1811.10748.
- 589 33. Jiang, P. et al. The fundamental performance of fast with 19-beam receiver at 1 band.
590 Research in Astronomy and Astrophysics **20**, 064 (2020).
- 591 34. Barsdell, B. R., Bailes, M., Barnes, D. G. & Fluke, C. J. Accelerating incoherent dedispersion.
592 Mon. Not. R. Astron. Soc. **422**, 379–392 (2012). 1201.5380.
- 593 35. Law, C. J. et al. A Distant Fast Radio Burst Associated with Its Host Galaxy by the Very Large
594 Array. Astrophys. J. **899**, 161 (2020). 2007.02155.
- 595 36. Law, C. J. rfpipeline: Radio interferometric transient search pipeline (2017). 1710.002.
- 596 37. Agarwal, D., Aggarwal, K., Burke-Spolaor, S., Lorimer, D. R. & Garver-Daniels, N. FETCH:
597 A deep-learning based classifier for fast transient classification. Mon. Not. R. Astron. Soc.
598 **497**, 1661–1674 (2020). 1902.06343.
- 599 38. Aggarwal, K. et al. Robust Assessment of Clustering Methods for Fast Radio Transient Can-
600 didates. Astrophys. J. **914**, 53 (2021). 2104.07046.
- 601 39. McMullin, J. P., Waters, B., Schiebel, D., Young, W. & Golap, K. CASA
602 Architecture and Applications. In Shaw, R. A., Hill, F. & Bell, D. J.

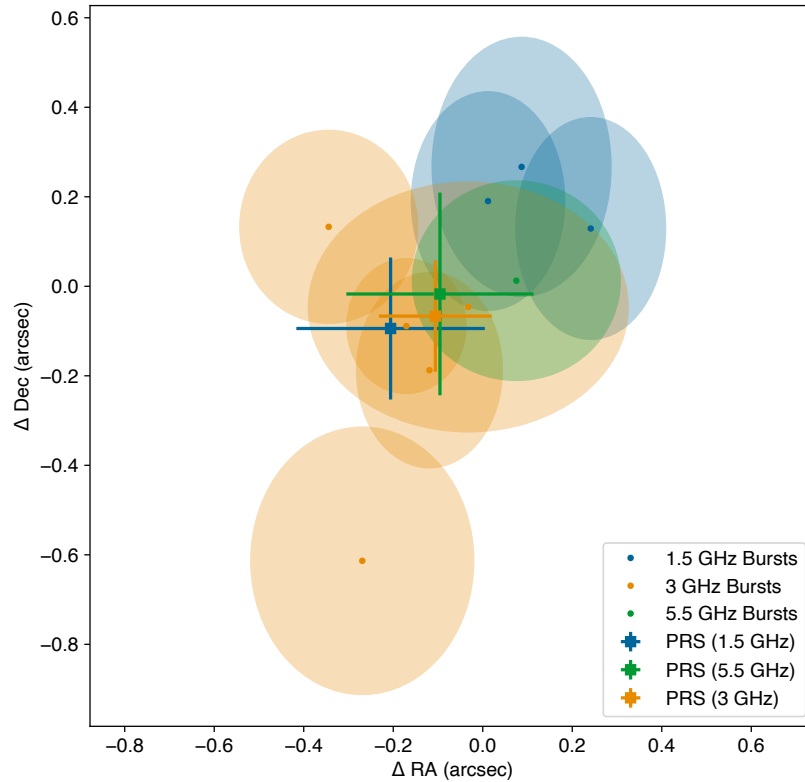
- 603 (eds.) Astronomical Data Analysis Software and Systems XVI, vol. 376 of
604 Astronomical Society of the Pacific Conference Series, 127 (2007).
- 605 40. Law, C. J. et al. A Multi-telescope Campaign on FRB 121102: Implications for the FRB
606 Population. ArXiv e-prints (2017). 1705.07553.
- 607 41. Aggarwal, K. et al. Comprehensive analysis of a dense sample of FRB 121102 bursts.
608 arXiv e-prints arXiv:2107.05658 (2021). 2107.05658.
- 609 42. Chambers, K. C. et al. The Pan-STARRS1 Surveys. arXiv e-prints arXiv:1612.05560 (2016).
610 1612.05560.
- 611 43. Oppermann, N., Yu, H.-R. & Pen, U.-L. On the non-Poissonian repetition pattern of
612 FRB121102. Mon. Not. R. Astron. Soc. **475**, 5109–5115 (2018). 1705.04881.
- 613 44. Yao, J. M., Manchester, R. N. & Wang, N. A New Electron-density Model for Estimation of
614 Pulsar and FRB Distances. Astrophys. J. **835**, 29 (2017). 1610.09448.
- 615 45. Shull, J. M. & Danforth, C. W. The Dispersion of Fast Radio Bursts from a Structured Inter-
616 galactic Medium at Redshifts $z < 1.5$. Astrophys. J. Lett. **852**, L11 (2018). 1712.01280.
- 617 46. Deng, W. & Zhang, B. Cosmological Implications of Fast Radio Burst/Gamma-Ray Burst
618 Associations. Astrophys. J. Lett. **783**, L35 (2014). 1401.0059.
- 619 47. Planck Collaboration et al. Planck 2018 results. XII. Galactic astrophysics using polarized
620 dust emission. Astron. & Astrophys. **641**, A12 (2020). 1807.06212.

- 621 48. Tendulkar, S. P. et al. The Host Galaxy and Redshift of the Repeating Fast Radio Burst FRB
622 121102. *Astrophys. J. Lett.* **834**, L7 (2017). 1701.01100.
- 623 49. Ocker, S. K., Cordes, J. M. & Chatterjee, S. Constraining Galaxy Haloes from the Dispersion
624 and Scattering of Fast Radio Bursts and Pulsars. arXiv e-prints arXiv:2101.04784 (2021).
625 2101.04784.
- 626 50. Michilli, D. et al. An extreme magneto-ionic environment associated with the fast radio burst
627 source FRB 121102. *Nature* **553**, 182–185 (2018). 1801.03965.
- 628 51. Hilmarsson, G. H. et al. Rotation Measure Evolution of the Repeating Fast Radio Burst Source
629 FRB 121102. arXiv e-prints arXiv:2009.12135 (2020). 2009.12135.

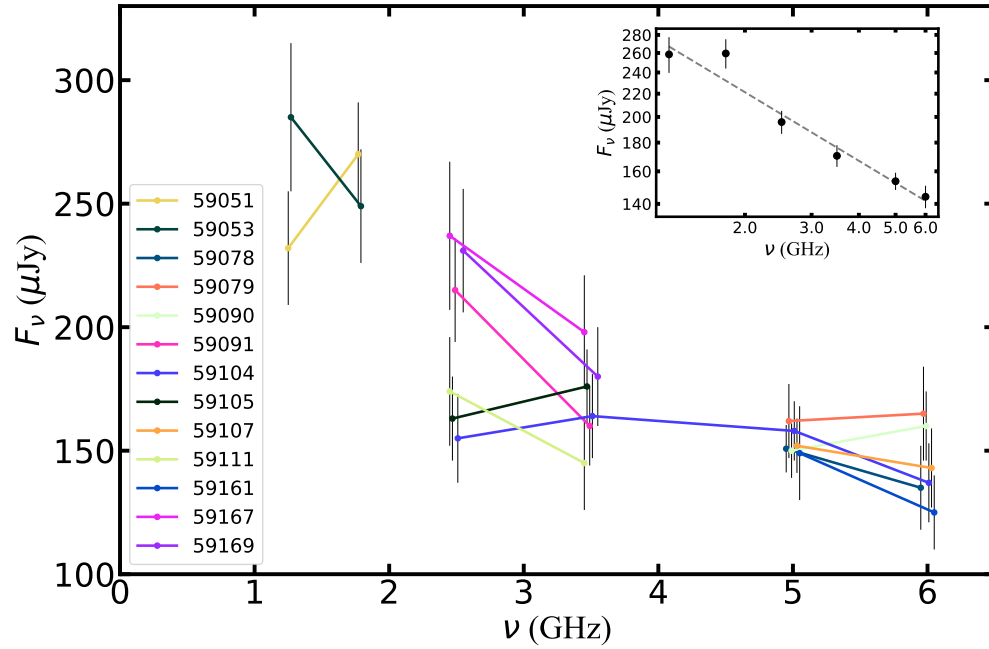
630 **Extended Data**



Extended Data | Figure 1 : **Measurements of the scattering timescale and statistics of pulse width.** Left and right plots exhibit the distribution of scattering timescale and pulse width, respectively.

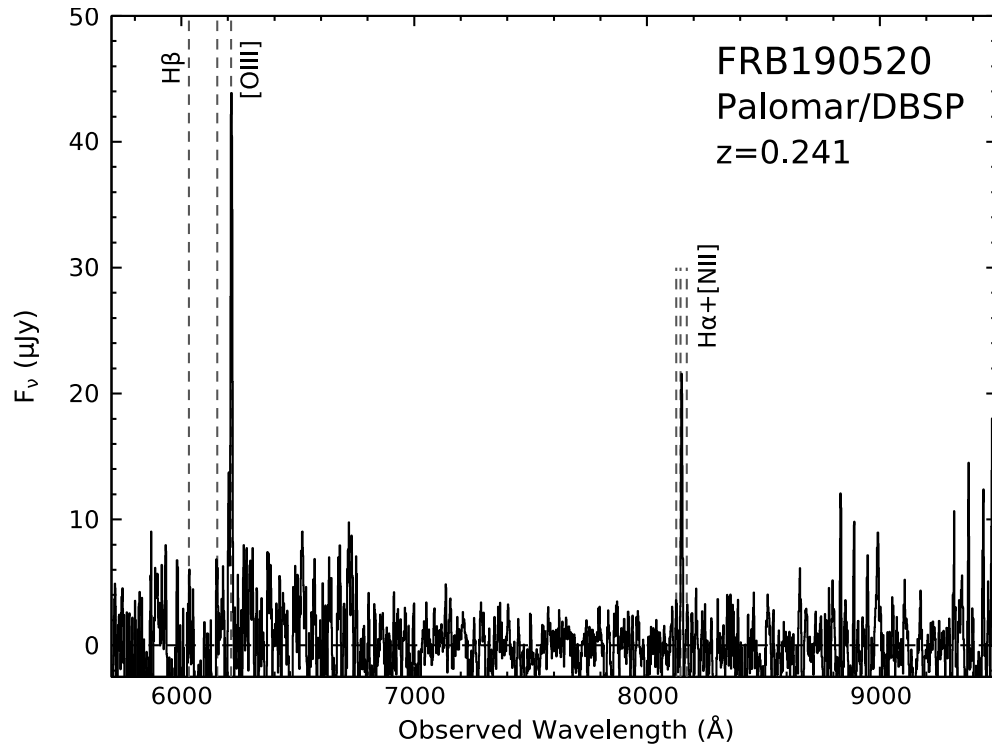


Extended Data | Figure 2 : Positions of the bursts and persistent radio source identified with VLA observations at 1.5, 3, and 5.5 GHz, shown as offsets from the best-fit position of the ensemble of bursts, at 16h02m04.2683s $-11^{\circ}17'17''.3203$ (J2000). The uncertainties on the positions of the bursts are indicated with shaded ellipses, and those for the PRS are shown with error bars. These uncertainties include 1σ statistical errors and estimates for systematic errors added in quadrature.



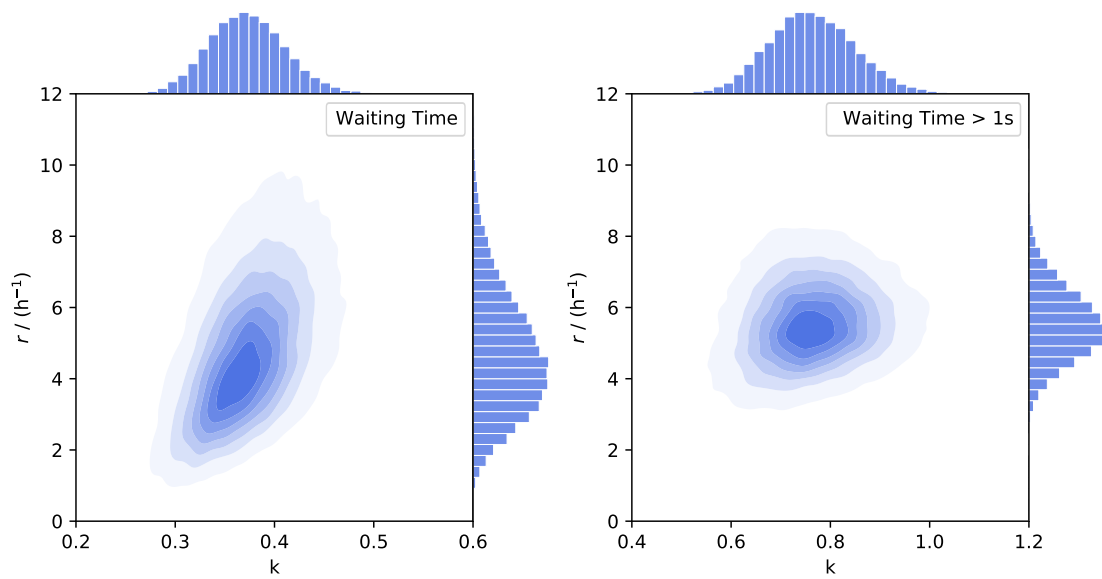
Extended Data | Figure 3 : **Spectral measurements of the PRS associated with FRB 190520.**

The bandwidth is split into two sub-bands for all the observations and the corresponding radio flux are shown. The frequencies for each sub-band are shifted slightly in order to show the flux error bars. The inset plot shows the average flux at each sub-band. By fitting a power-law model to these measurements, which is shown by the black dashed line, we derived the spectral index of the PRS as -0.41 ± 0.04 .



Extended Data | Figure 4 : Palomar DBSP optical spectrum of the FRB 190520 host galaxy.

The redshift of $z = 0.241$ was determined with well-detected [OIII]-5007 \AA line and H α line ($> 5\sigma$). Two emission lines are narrow, with FWHM $\sim 10 \text{\AA}$. The flux scale of the spectrum is not corrected for the slit loss.



Extended Data | Figure 5 : Posterior probability distribution for shape parameters k and event rate r of the Weibull distribution. Left panel: fit to all waiting times of FRB 190520 from FAST. Right panel: fit to the waiting times longer than 1 s.

Extended Data | Table 1 : The properties of the 79 FRB 190520

bursts detected by FAST.

Burst ID	Burst time (MJD)	DM (pc cm ⁻³)	Pulse Width (ms)	Bandwidth (MHz)	Scatter tail (ms)	Fluence (mJy ms)	Energy (×10 ³⁷ erg)
1	58623.716958197	1226.3 (6.0)	8.7 (0.8)	1300-1450	-	75.0 (3.0)	9.1 (0.4)
2	58623.716997034	1226.3 (6.0)	16.4 (0.6)	1050-1250	-	30.0 (2.0)	3.6 (0.2)
3	58623.717075743	1226.3 (6.0)	7.1 (0.8)	1300-1450	-	53.0 (3.0)	6.4 (0.4)
4	58623.717421629	1226.3 (6.0)	7.3 (1.0)	1050-1450	-	51.0 (4.0)	6.2 (0.5)
5	58963.766862939	1202.8 (12.8)	10.4 (0.3)	1300-1450	-	66.0 (7.0)	8.0 (0.8)
6	58963.790991383	1202.8 (12.8)	10.2 (1.8)	1300-1450	13.1(2.4)	53.0 (5.0)	6.4 (0.7)
7	58991.684351079	1200.4 (10.4)	20.3 (0.4)	1300-1450	-	107.0 (19.0)	13.0 (2.2)
8	58991.686137870	1200.4 (10.4)	22.8 (8.4)	1360-1450	11.5(6.9)	100.0 (11.0)	12.2 (1.3)
9	58991.686875951	1200.4 (10.4)	9.2 (0.3)	1300-1450	-	81.0 (13.0)	9.8 (1.5)
10	58991.704636888	1200.4 (10.4)	19.5 (1.8)	1350-1450	3.6(0.9)	108.0 (12.0)	13.1 (1.5)
11	58991.704638485	1200.4 (10.4)	9.7 (0.8)	1370-1450	-	43.0 (1.0)	5.2 (0.1)
12	58991.717697335	1200.4 (10.4)	11.9 (1.1)	1300-1450	10.3(1.2)	123.0 (21.0)	14.9 (2.6)
13	58991.717878516	1200.4 (10.4)	14.3 (4.0)	1200-1450	5.1(2.6)	59.0 (11.0)	7.1 (1.3)
14	58991.718217265	1200.4 (10.4)	11.8 (1.5)	1360-1450	-	64.0 (7.0)	7.7 (0.8)
15	58991.718217670	1200.4 (10.4)	17.5 (0.3)	1360-1450	-	39.0 (4.0)	4.8 (0.5)
16	58991.718218082	1200.4 (10.4)	20.2 (2.2)	1270-1450	12.6(1.9)	153.0 (28.0)	18.6 (3.4)
17	58991.735450006	1200.4 (10.4)	30.2 (0.5)	1300-1450	-	139.0 (22.0)	16.8 (2.6)
18	58991.750640038	1200.4 (10.4)	17.7 (1.3)	1300-1450	-	61.0 (9.0)	7.4 (1.2)
19	58991.750640790	1200.4 (10.4)	20.2 (0.6)	1200-1450	-	81.0 (14.0)	9.9 (1.8)
20	59060.484475154	1201.5 (11.5)	13.5 (1.4)	1300-1450	11.3(1.4)	241.0 (13.0)	29.3 (1.6)
21	59060.507858658	1201.5 (11.5)	7.3 (1.0)	1300-1450	9.3(1.3)	170.0 (9.0)	20.7 (1.1)
22	59060.525960600	1201.5 (11.5)	17.3 (2.4)	1150-1450	7.6(1.7)	168.0 (15.0)	20.3 (1.8)
23	59061.512755579	1201.5 (11.5)	8.5 (0.1)	1300-1450	-	48.0 (6.0)	5.9 (0.8)
24	59061.512755780	1201.5 (11.5)	10.0 (2.3)	1280-1450	4.7(1.8)	129.0 (17.0)	15.7 (2.0)
25	59061.516277966	1201.5 (11.5)	7.1 (0.7)	1350-1450	-	30.0 (3.0)	3.6 (0.3)
26	59061.516278904	1201.5 (11.5)	7.5 (0.4)	1300-1450	-	49.0 (6.0)	6.0 (0.7)
27	59061.516279436	1201.5 (11.5)	11.4 (0.8)	1350-1450	-	49.0 (5.0)	6.0 (0.6)
28	59061.524341261	1201.5 (11.5)	10.7 (0.8)	1300-1450	10.4(1.0)	122.0 (16.0)	14.8 (2.0)

Extended Data | Table 1 : The properties of the 79 FRB 190520

bursts detected by FAST.

Burst ID	Burst time (MJD)	DM (pc cm ⁻³)	Pulse Width (ms)	Bandwidth (MHz)	Scatter tail (ms)	Fluence (mJy ms)	Energy (×10 ³⁷ erg)
29	59061.535633328	1201.5 (11.5)	14.0 (0.4)	1350-1450	-	84.0 (8.0)	10.2 (1.0)
30	59061.536568858	1201.5 (11.5)	21.9 (19.0)	1300-1450	-	72.0 (9.0)	8.7 (1.1)
31	59061.536569628	1201.5 (11.5)	19.0 (1.4)	1100-1450	14.0(1.3)	122.0 (42.0)	14.8 (5.0)
32	59061.537903820	1201.5 (11.5)	23.9 (2.7)	1300-1450	4.9(1.4)	66.0 (8.0)	8.0 (1.0)
33	59061.539298603	1201.5 (11.5)	9.9 (0.3)	1300-1450	-	74.0 (9.0)	8.9 (1.1)
34	59061.541828100	1201.5 (11.5)	19.8 (2.0)	1050-1200	8.7(1.0)	212.0 (28.0)	25.8 (3.4)
35	59067.467544345	1201.9 (10.5)	15.2 (7.6)	1200-1400	5.4(4.6)	67.0 (8.0)	8.2 (1.0)
36	59067.486738799	1201.9 (10.5)	14.9 (2.3)	1300-1450	17.8(2.9)	131.0 (14.0)	15.9 (1.7)
37	59067.486739378	1201.9 (10.5)	33.1 (0.7)	1050-1300	-	147.0 (18.0)	17.8 (2.2)
38	59067.502691880	1201.9 (10.5)	14.3 (0.7)	1120-1220	-	135.0 (3.0)	16.3 (0.4)
39	59067.509899127	1201.9 (10.5)	12.2 (1.8)	1250-1400	10.3(1.8)	122.0 (8.0)	14.8 (1.0)
40	59067.535246460	1201.9 (10.5)	7.6 (0.3)	1300-1450	-	74.0 (10.0)	9.0 (1.2)
41	59069.495909561	1201.9 (10.5)	16.8 (0.5)	1270-1450	-	143.0 (11.0)	17.4 (1.3)
42	59069.501196109	1201.9 (10.5)	18.7 (0.1)	1300-1450	-	292.0 (15.0)	35.4 (1.8)
43	59069.514994796	1201.9 (10.5)	12.2 (1.6)	1300-1450	11.6(1.7)	193.0 (13.0)	23.4 (1.6)
44	59071.472522775	1201.9 (10.5)	5.2 (0.3)	1340-1450	-	79.0 (2.0)	9.6 (0.2)
45	59071.472523007	1201.9 (10.5)	7.2 (0.8)	1340-1450	-	67.0 (2.0)	8.1 (0.2)
46	59071.491696655	1201.9 (10.5)	10.4 (2.0)	1300-1450	4.9(1.6)	185.0 (5.0)	22.4 (0.6)
47	59073.496887082	1200.0 (8.0)	7.8 (0.2)	1250-1450	-	108.0 (10.0)	13.1 (1.2)
48	59073.515256071	1200.0 (8.0)	18.7 (0.7)	1350-1450	-	148.0 (2.0)	17.9 (0.2)
49	59073.515256881	1200.0 (8.0)	11.1 (0.7)	1160-1360	-	58.0 (5.0)	7.0 (0.6)
50	59075.454353002	1200.0 (8.0)	24.9 (0.1)	1050-1180	-	313.0 (19.0)	38.0 (2.4)
51	59075.454862469	1200.0 (8.0)	22.0 (0.1)	1250-1450	-	210.0 (13.0)	25.5 (1.6)
52	59075.472181012	1200.0 (8.0)	14.0 (0.6)	1260-1400	-	114.0 (7.0)	13.8 (0.8)
53	59075.484186304	1200.0 (8.0)	6.0 (0.1)	1100-1400	-	158.0 (16.0)	19.1 (2.0)
54	59075.496463775	1200.0 (8.0)	16.7 (0.4)	1150-1450	-	84.0 (8.0)	10.1 (1.0)
55	59077.448938437	1200.0 (8.0)	11.9 (0.6)	1200-1400	-	103.0 (7.0)	12.5 (0.8)
56	59077.448939131	1200.0 (8.0)	14.4 (0.8)	1250-1450	-	108.0 (6.0)	13.1 (0.7)
57	59077.449538432	1200.0 (8.0)	13.4 (1.8)	1280-1400	10.6(1.7)	199.0 (10.0)	24.2 (1.3)

Extended Data | Table 1 : The properties of the 79 FRB 190520

bursts detected by FAST.

Burst ID	Burst time (MJD)	DM (pc cm ⁻³)	Pulse Width (ms)	Bandwidth (MHz)	Scatter tail (ms)	Fluence (mJy ms)	Energy (×10 ³⁷ erg)
58	59077.449939184	1200.0 (8.0)	39.1 (0.5)	1280-1450	-	149.0 (7.0)	18.0 (0.9)
59	59077.449939372	1200.0 (8.0)	38.0 (0.6)	1050-1450	-	121.0 (12.0)	14.7 (1.4)
60	59077.460100338	1200.0 (8.0)	13.0 (2.4)	1300-1450	13.5(2.8)	132.0 (2.0)	16.1 (0.2)
61	59077.460503968	1200.0 (8.0)	10.3 (1.9)	1250-1450	10.6(2.1)	94.0 (5.0)	11.4 (0.6)
62	59077.466295203	1200.0 (8.0)	11.7 (0.3)	1250-1400	-	157.0 (10.0)	19.0 (1.2)
63	59077.468715062	1200.0 (8.0)	18.4 (3.5)	1050-1250	7.6(1.8)	129.0 (9.0)	15.6 (1.1)
64	59077.469903193	1200.0 (8.0)	11.2 (1.1)	1250-1450	11.3(1.3)	152.0 (7.0)	18.5 (0.9)
65	59077.475047947	1200.0 (8.0)	11.0 (1.7)	1200-1450	8.3(1.6)	107.0 (7.0)	13.0 (0.8)
66	59077.475330491	1200.0 (8.0)	14.0 (0.8)	1250-1450	12.9(0.9)	205.0 (12.0)	24.9 (1.4)
67	59077.477447949	1200.0 (8.0)	2.0 (0.2)	1300-1450	-	70.0 (3.0)	8.5 (0.3)
68	59077.485451841	1200.0 (8.0)	14.3 (0.2)	1340-1450	-	333.0 (7.0)	40.4 (0.9)
69	59077.485451957	1200.0 (8.0)	14.4 (0.2)	1270-1450	-	262.0 (16.0)	31.8 (1.9)
70	59077.490027004	1200.0 (8.0)	8.4 (0.4)	1350-1450	-	132.0 (3.0)	16.1 (0.3)
71	59077.491413589	1200.0 (8.0)	10.3 (0.3)	1300-1450	-	115.0 (5.0)	14.0 (0.6)
72	59077.497806611	1200.0 (8.0)	15.3 (2.2)	1200-1450	10.7(2.1)	138.0 (10.0)	16.8 (1.2)
73	59077.497957805	1200.0 (8.0)	13.6 (0.5)	1200-1450	-	89.0 (6.0)	10.9 (0.7)
74	59077.498960966	1200.0 (8.0)	4.6 (0.8)	1200-1450	11.8(1.5)	94.0 (6.0)	11.4 (0.7)
75	59089.428163703	1200.5 (8.8)	11.2 (0.3)	1300-1450	-	112.0 (3.0)	13.6 (0.4)
76	59089.436165435	1200.5 (8.8)	13.3 (0.7)	1350-1450	-	83.0 (3.0)	10.1 (0.3)
77	59111.370525959	1201.0 (11.0)	20.6 (0.7)	1360-1450	-	99.0 (12.0)	12.0 (1.4)
78	59111.370526098	1201.0 (11.0)	6.7 (0.2)	1250-1450	-	106.0 (8.0)	12.9 (1.0)
79	59111.370978062	1201.0 (11.0)	14.6 (0.5)	1350-1450	-	98.0 (10.0)	11.9 (1.2)

Start Time (MJD)	Frequency (GHz)	Duration (min)	Beam size (“,“)	Flux density (μ Jy)	Bursts
59051.033815	1.5	96	4.78×2.90	258±16	1
59053.046790	1.5	96	4.63×2.90	273±23	2
59079.004955	5.5	41	1.38×1.02	145±10	0
59079.971533	5.5	41	1.44×1.05	164±11	0
59090.941498	5.5	41	1.45×1.04	158±9	0
59091.938768	3	41	2.43×1.85	195±14	5
59104.867225	3	41	2.76×1.76	160±13	0
59104.908789	5.5	41	1.43×1.04	151±9	0
59105.976837	3	41	2.44×1.60	186±15	0
59107.915546	5.5	41	1.38×1.02	153±10	1
59111.116215	3	41	5.00×1.45	176±16	0
59161.677240	5.5	41	1.92×0.47	139±13	0
59167.637761	3	41	2.76×0.51	233±17	0
59169.640486	3	41	2.47×0.48	211±14	-

Extended Data | Table 2 : Details of our VLA observations of the PRS and the number of bursts detected in each observation. Note that the *realfast* system wasn't run on the last observation due to a system error.

Frequency (GHz)	RA	Dec	Statistical Error		Systematic Offsets	
			RA (“)	Dec (“)	RA (“)	Dec (“)
1.5	16h02m04.2543s	-11d17m17.4146s	0.0386	0.0713	0.0137±0.1539	-0.0201±0.1981
3	16h02m04.2611s	-11d17m17.3869s	0.0176	0.0168	-0.0187±0.1232	0.0232±0.1249
5.5	16h02m04.2618s	-11d17m17.3375s	0.0075	0.0095	-0.0947±0.2263	0.1069±0.2090

Extended Data | Table 3 : Localised positions of the PRS from 1.5, 3, 5.5 GHz VLA deep images. The first column shows the observing central frequency. The second and third columns report the coordinates of the PRS from the deep images. The remaining columns show the 1σ statistical errors and the cross-matched systematic offsets in ra. and dec..

Band	SNR	DM (pc cm ⁻³)	RA	Dec	Statistical Error		Systematic Error	
					RA (")	Dec (")	RA (")	Dec (")
L1	15.45	1209.60	16h02m04.2742s	-11d17m17.0535s	0.124	0.208	0.1539	0.1981
L2	26.68	1227.15	16h02m04.2847s	-11d17m17.1912s	0.060	0.145	0.1539	0.1981
L3	15.26	1236.60	16h02m04.2691s	-11d17m17.1299s	0.070	0.139	0.1539	0.1981
S1	18.93	1291.30	16h02m04.2567s	-11d17m17.4093s	0.044	0.080	0.1232	0.1249
S2	16.87	1193.40	16h02m04.2449s	-11d17m17.1874s	0.153	0.173	0.1232	0.1249
S3	15.40	1222.75	16h02m04.2602s	-11d17m17.5078s	0.103	0.176	0.1232	0.1249
S4	9.93	1216.80	16h02m04.2661s	-11d17m17.3666s	0.333	0.247	0.1232	0.1249
S5	6.70	1276.50	16h02m04.25s	-11d17m17.9337s	0.214	0.269	0.1232	0.1249
C1	19.03	1267.50	16h02m04.2734s	-11d17m17.3078s	0.041	0.071	0.2263	0.2090

Extended Data | Table 4 : Localised positions of the VLA bursts. The alphabet in the first column shows the frequency band of observation, followed by the burst number. Second column reports the image signal to noise ratio. The remaining columns show the burst positions (and errors) obtained using CASA calibration and image fitting.

Name	MJD	DM	Width (ms)	Fluence (Jy ms)	Center (GHz)	FWHM (MHz)
L1	59051.05154282(9)	1222(8)	13(2)	4(6)	1.7(2)	348(287)
L2	59053.10828443(6)	1246(6)	15.4(8)	3.9(3)	1.703(4)	157(14)
L3	59053.10103193(2)	1240(11)	11(2)	1.8(3)	1.75(1)	249(41)
S1	59091.96051286(4)	1271(14)	12(2)	1.3(2)	3.13(6)	951(138)
S2	59091.95616141(2)	1104(38)	5(1)	0.63(5)	3.751(8)	239(24)
S3	59091.96358084(4)	1185(8)	0.8(9)	2.3(1)	2.63(1)	344(15)
S4	59091.94361231(2)	1262(43)	0.7(6)	0.35(4)	3.50(3)	534(74)
S5	59091.96692835(6)	1279(16)	4(3)	< 4(1)	–	–
C1	59107.92580416(1)	1281(218)	0.11(7)	0.36(3)	5.266(9)	228(26)

Extended Data | Table 5 : Spectro-temporal properties of the VLA bursts. The (1 σ) errors on the last digit are shown in parenthesis.